Inorganic Chemistry

Article

pubs.acs.org/IC

Protonation of a Peroxodiiron(III) Complex and Conversion to a Diiron(III/IV) Intermediate: Implications for Proton-Assisted O−O Bond Cleavage in Nonheme Diiron Enzymes

Matthew A. Cranswick,[†] Katlyn K. Meier,[‡] Xiaopeng Shan,[†] Audria Stubna,[‡] Józef Kaizer,[†] Mark P. Mehn,[†] Eckard Münck,*[,‡] and Lawrence Que, Jr.*[,†]

[†]Department of Chemistry and Center for Metals in Biocatalysis, University of Minnesota, Minneapolis, Minnesota 55455, United States

[‡]Department of Chemistry, Carnegie Mellon University, Pittsburgh, Pennsylvania 15213, United States

Supporting Information

ABSTRACT: Oxygenation of a diiron(II) complex, $[Fe^{II}_2(\mu\text{-}OH)_2(BnBQA)_2(NCMe)_2]^{2+}$ [**2**, where BnBQA is *N*-benzyl-*N*,*N*-bis(2-quinolinylmethyl)amine], results in the formation of a metastable peroxodiferric intermediate, **3**. The treatment of **3** with strong acid affords its conjugate acid, **4**, in which the (μ-oxo)(μ-1,2-peroxo)diiron(III) core of **3** is protonated at the oxo bridge. The core structures of **3** and **4** are characterized in detail by UV−vis, Mössbauer, resonance Raman, and X-ray absorption spectroscopies. Complex **4** is shorter-lived than **3** and decays to generate in ∼20% yield of a diiron(III/IV) species **5**, which can be identified by electron paramagnetic resonance and Mössbauer spectroscopies. This reaction sequence demonstrates for the first time that protonation of the oxo bridge of a (μ-oxo)(μ-1,2-peroxo)diiron(III) complex leads to cleavage of the peroxo O−O bond and formation of a high-valent diiron complex, thereby mimicking the steps involved in the formation of intermediate X in the activation cycle of ribonucleotide reductase.

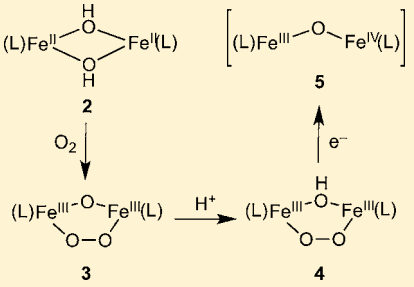

INTRODUCTION

Dioxygen (O_2) activation at a nonheme diiron active site is a key step for a number of biologically important transformations, including the hydroxylation of CH_4 by soluble methane monooxygenase (sMMO) and related reactions by bacterial multicomponent monooxygenases,[1−4] the control of eukaryotic cell proliferation by human deoxyhypusine hydroxylase (hDOHH),[5] the biosynthesis of the antibiotic chloramphenicol by CmlI/CmlA,[6] and the conversion of ribonucleotides to deoxyribonucleotides by ribonucleotide reductase (RNR),[7] to name a few. In general, O_2 activation proceeds via binding of O_2 to the diferrous active site to form a peroxodiferric intermediate. In sMMO and RNR, the O−O bond of the peroxodiferric intermediate is activated via proton and/or electron transfer (PT and ET, respectively) to yield a high-valent intermediate responsible for their respective oxidative functions.[8−11] The high-valent intermediate of sMMO, known as Q, has been shown to contain a $[Fe^{IV}_2(O)_2]$ "diamond" core structure,[12] a notion supported by recent computational studies.[13−17] In RNR R2, ET from a nearby tryptophan residue to the peroxodiferric intermediate triggers O−O bond cleavage, leading to the formation of a mixed-valent $[Fe^{III}−O−Fe^{IV}]$ intermediate, X, which generates the catalytically essential tyrosyl radical.[18,19]

To date, peroxodiferric intermediates have been trapped and spectroscopically characterized for sMMO,[20−22] *Escherichia coli* W48F/D84E RNR R2,[23−26] mouse RNR R2,[27] the ferroxidase center of frog M ferritin,[28,29] stearoyl acyl carrier protein Δ^9D desaturase (Δ^9D),[30,31] toluene/*o*-xylene monooxygenase hydroxylase,[32,33] and hDOHH,[5] which exhibit lifetimes ranging from milliseconds to days. Resonance Raman (rRaman) studies of some of these intermediates reveal ν(O−O) frequencies of 851−898 cm^{-1} and ν_{sym}(Fe−O_2−Fe) frequencies of 442−485 cm^{-1}, the analysis of which has led investigators to favor a *cis*-μ-1,2-O_2 binding mode.[26,34,35] The stability of the peroxodiferric intermediate is also likely to be modulated by the nature of the bridging iron ligands, as well as active site residues that may play a crucial role in facilitating the proton-assisted cleavage of the O−O bond.

Suitable model compounds can provide insight into these factors. Indeed, in the past 20 years, many synthetic peroxodiferric complexes have been trapped and spectroscopically characterized from the reactions of diiron(II) precursors with O_2 or diiron(III) complexes with H_2O_2.[27,36−51] Some of these intermediates are stable enough to have been crystallized, and the crystal structures of five such complexes have been reported.[39−41,45] In each case, there is a (*cis*-μ-1,2-peroxo)-diferric center that is supported by one or two additional bridging groups such as oxo, hydroxo, alkoxo, and/or a bidentate carboxylate, which constrain the Fe···Fe distances to a range from 3.2 to 4 Å (Table 1). The relative stability of these

Received: July 26, 2012
Published: September 12, 2012

Table 1. Properties of the Peroxodiferric Units in Synthetic Complexes and Enzymes

peroxo intermediate[a]	λ_{max}, nm (ε, M^{-1} cm^{-1})	δ (ΔE_Q), mm s^{-1}	J, cm^{-1}	ν(O−O), cm^{-1}	d(Fe···Fe), Å	ref
3	505 (1250) 650 (1300)	0.55 (1.43)	>120	854	3.16	this work
4	730 (2400)	0.57 (−1.35), 0.56 (−0.96)	80(15)	925	3.46	this work
A	494 (1100) 648 (1200)	0.54 (1.68)		848	3.14	54
B	510 (1300) 610 (1310)	0.53 (1.67)	110	815 or 830	3.04	47, 49
C	577 (1500)	0.50 (1.46)		847	3.171(1)	45
C′	644 (3000)	0.50 (1.31)		908	3.396(1)	45
HPTB-1	588 (1500)			900	3.462(3)	39, 49
HPTB-2	686 (2200)	0.56 (−1.26)	57(7)	849	3.25	50
HPTB-3	590 (2200)	0.53 (1.03)	60(10)	897	3.47	50
Ph-bimp	500−800 br (1700)	0.58 (0.74), 0.65 (1.70)		884[b]	3.327(2)	40
Tp	675 (1500)	0.66 (1.40)	66	876	4.000(4)	38, 41
hDOHH	630 (2800)	0.55 (1.16), 0.58 (0.88)	60(10)	855	3.44	5
Δ^9D	700 (1100)	0.68 (1.90), 0.64 (1.06)		898		30, 31
W48F/D84E RNR	700 (1800)	0.63 (1.58)	50(10)	870	2.50 (XAS),[c] 3.68 (rR/DFT)	23−26, 29
frog M ferritin	650 (1000)	0.62 (1.06)	75(10)	851	2.53 (XAS)	28, 29, 56
sMMO H_{peroxo}	725 (1800)	0.66 (1.51)				21, 22

[a] **A** = $[Fe^{III}_2(\mu\text{-}O)(\mu\text{-}O_2)(6\text{-}Me_3TPA)_2]^{2+}$ [6-Me_3TPA = tris(6-methyl-2-pyridylmethyl)amine]; **B** = $[Fe^{III}_2(\mu\text{-}O)(\mu\text{-}O_2)(\mu\text{-}O_2CMe)(BPPE)_2]^{2+}$ {BPPE = 1,2-bis[2-(bis(2-pyridyl)methyl)-6-pyridyl]ethane}; **C** = $[Fe^{III}_2(\mu\text{-}O)(\mu\text{-}O_2)(6\text{-}Me_2BPP)_2]^{2+}$ [6-Me_2BPP = bis(6-methyl-2-pyridylmethyl)-3-aminopropionate]; **C′** = $[Fe^{III}_2(\mu\text{-}OH)(\mu\text{-}O_2)(6\text{-}Me_2\text{-}BPP)_2]^{3+}$; **HPTB-1** = $[Fe^{III}_2(\mu\text{-}O_2)$(N-Et-HPTB)$(OPPh_3)_2]^{3+}$ [N-Et-HPTB = tetrakis(2-benzimidazolylmethyl)-2-hydroxy-1,3-diaminopropane]; **HPTB-2** = $[Fe^{III}_2(\mu\text{-}O_2)(\mu\text{-}O_2PPh_2)$(N-Et-HPTB)$]^{2+}$; **HPTB-3** = $[Fe^{III}_2(O_2)$(N-Et-HPTB)$(\eta^1\text{-}O_2PPh_2)$(NCMe)$]^{2+}$; **Ph-bimp** = $[Fe^{III}_2(\mu\text{-}1,2\text{-}O_2)(\mu\text{-}O_2CCH_3)$(Ph-bimp)$]^{2+}$ {Ph-bimp = 2,6-bis[bis[2-(1-methyl-4,5-diphenylimidazolyl)methyl]aminomethyl]-4-methylphenolate}; **Tp** = $[Fe^{III}_2(\mu\text{-}O_2)(Tp^{iPr2})_2(\mu\text{-}O_2CCH_2Ph)_2]$ [Tp^{iPr2} = tris(3,5-diisopropyl-1-pyrazolyl)borate]. [b]The frequency was obtained for the related complex $[Fe_2(\mu\text{-}1,2\text{-}O_2)(\mu\text{-}O_2CCH_3)(L)]^{2+}$ [L = *N*,*N*′-(2-hydroxy-5-methylxylylene)bis(*N*-carboxymethylglycine)].[55] [c]Unresolved disagreement in the deduced Fe···Fe distance.

peroxo intermediates has allowed their structural and spectroscopic properties to be determined and used to shed light on the nature of the corresponding enzyme intermediates.

However, much less insight has been gained into how O−O bond cleavage can be promoted, the next key step in the catalytic cycles of the enzymes. Of all of the synthetic peroxo intermediates characterized thus far, in only two cases has the peroxo intermediate been shown to be directly involved in substrate oxidation.[42,48] In the first example, intramolecular hydroxylation of a pendant phenyl group on the dinucleating ligand is observed upon decay of the intermediate, while in the second example, the oxidation of a variety of added substrates is seen, but only if the substrates can coordinate to the diiron center. In two other examples, Lewis acid activation by a proton[52] or an acyl chloride[53] was required to elicit oxidative reactivity from the peroxo intermediate. No further insights into how the O−O bond was activated were obtained in these studies. Thus, finding more examples of well-defined peroxodiferric complexes that allow investigation of the O−O bond cleavage step can enhance opportunities to gain insight into the factors that control this crucial step in the activation of O_2 at nonheme diiron centers.

Protons have been found to play a role in facilitating O−O bond cleavage of the peroxodiferric intermediates of sMMO[8,9] and hDOHH[5] to generate species capable of oxidizing substrates. To shed light on how protons aid in the cleavage of the O−O bond and the formation of a high-valent diiron center, we describe herein studies on the protonation of a metastable $[Fe^{III}_2(\mu\text{-}O)(\mu\text{-}1,2\text{-}O_2)]$ complex. On the basis of a detailed spectroscopic characterization, protonation is shown to occur at the oxo bridge, generating a $[Fe^{III}_2(\mu\text{-}OH)(\mu\text{-}1,2\text{-}O_2)]$ complex, which, in turn, decays to form a $[Fe^{III}\text{−}O\text{−}Fe^{IV}]$ complex, which serves as a model for high-valent intermediate X in the activation cycle of diiron-containing RNR.

EXPERIMENTAL SECTION

General Considerations. All reagents were purchased from commercial vendors and used as received, unless noted otherwise. $^{18}O_2$ (90%) and $H_2{}^{18}O$ (97%) were purchased from Cambridge Isotopes. *N*-benzyl-*N*,*N*-bis(2-quinolinylmethyl)amine (BnBQA)[44] and $[Fe^{II}(NCCH_3)_2(OTf)_2]$[57] were prepared following previously published procedures. $[Fe^{II}$(BnBQA)$(NCMe)(OTf)_2]$ (**1**) was prepared as reported by Kryatov et al.,[44] with the exception that $[Fe^{II}(NCCH_3)_2(OTf)_2]$ was used as the iron salt and the reaction was carried out in MeCN. Recrystallization of **1** was achieved by dissolution of the complex in MeCN and layering with excess Et_2O. $[Fe^{II}_2(\mu\text{-}OH)_2$(BnBQA)$_2(NCMe)_2](OTf)_2$ (**2**) was also prepared using the general procedures outlined by Kryatov et al.[44] by first generating **1** and subsequently adding 1 equiv of H_2O in MeCN, followed by 1 equiv of Et_3N in MeCN.

All moisture- and oxygen-sensitive compounds were prepared using standard vacuum-line, Schlenk, or cannula techniques. A nitrogen-filled glovebox was used for any subsequent manipulation and storage of these compounds. Electronic spectroscopic measurements were performed using a HP8453A diode-array spectrometer equipped with a cryostat from Unisoku Scientific Instruments (Osaka, Japan). Electrospray ionization mass spectrometry (ESI-MS) experiments were carried out on a Bruker BioTOF II mass spectrometer using a spray chamber voltage of 4000 V and a carrier gas temperature between 100 and 200 °C depending on the stability of the complex. The samples were kept at −40 °C during sample collection using an EtOH/CO_2 bath.

Physical Methods. *rRaman Spectroscopy.* rRaman spectra were collected using Spectra-Physics model 2060 Kr^+ and 2030-15 Ar^+ lasers and an Acton AM-506 monochromator equipped with a Princeton LN/CCD data collection system. Low-temperature spectra in CH_3CN or CD_3CN were obtained at 77 K using a 135° backscattering geometry. Samples were frozen onto a gold-plated copper coldfinger in thermal contact with a dewar flask containing liquid nitrogen. Raman frequencies were calibrated to indene prior to data collection. Rayleigh scattering was attenuated using a holographic notch filter (Kaiser Optical Systems) for each excitation wavelength. The monochromator slit width was set for a band pass of 4 cm^{-1} for all spectra. The spectra of **3** were collected using a laser excitation power

of 100 mW, whereas the spectra of **4** were collected using a maximum excitation power of 40 mW. The plotted spectra are averages of 32 scans with collection times of 30 s. All spectra were intensity-corrected to the 710 and 773 cm^{-1} solvent peak of CD_3CN and CH_3CN, respectively.

X-ray Absorption Spectroscopy (XAS). Data Collection. XAS data were collected on Beamline 7-3 of the Stanford Synchrotron Radiation Lightsource (SSRL) at the SLAC National Accelerator Laboratory. Fe K-edge XAS data were collected for frozen samples prepared in either tandem XAS/Mössbauer cups or SSRL solution cells with $[Fe]_T \sim 6$ mM. The SPEAR storage ring was operated at 3.0 GeV and ~350 mA, and energy resolution of the focused incoming X-rays was achieved using a Si(220) double-crystal monochromator, which was detuned to 50% of the maximal flux to attenuate second-harmonic X-rays. The sample temperature (7–10 K) was controlled utilizing an Oxford Instruments CF1208 continuous-flow liquid-helium cryostat. Harmonic rejection was achieved by a 9 keV cutoff filter. Data were obtained as fluorescence excitation spectra with a 30-element solid-state germanium detector array (Canberra). In fluorescence mode, photon scattering "noise" was reduced using a 3 μm manganese filter and a Soller slit. An iron foil spectrum was recorded concomitantly for internal energy calibration, and the first inflection point of the K-edge was assigned to 7112.0 eV. The edge energies were routinely monitored during data collection for red shifts indicative of sample photoreduction, but none were observed in the present study.

Data Analysis. Data reduction, averaging, and normalization were performed using the program *EXAFSPAK*.[58] The data for **3** and **4** are the average of 10 and 13 data sets, respectively. Following calibration and averaging of the data, background absorption was removed by fitting a Gaussian function to the preedge region and then subtracting this function from the entire spectrum. A three-segment spline with fourth-order components was then fit to the EXAFS region of the spectrum in order to extract $\chi(k)$.

Theoretical phase and amplitude parameters for a given absorber–scatterer pair were calculated using *FEFF 8.40* and were utilized by the "opt" program of the *EXAFSPAK* package during curve fitting. Parameters for **3** and **4** were calculated using similar coordinates of the available crystal structures of the conjugate acid–base complexes reported by Zhang et al.[45] In all analyses, the coordination number of a given shell was a fixed parameter and was varied iteratively in integer steps, while the bond lengths (r) and mean-square deviation (σ^2) were allowed to freely float. The amplitude reduction factor S_0 was fixed at 0.9, while the edge-shift parameter E_0 was allowed to float as a single value for all shells. Thus, in any given fit, the number of floating parameters was typically equal to (2 × num shells) + 1. The goodness of fit F was defined simply as $\sum(\chi_{exptl} - \chi_{calc})^2$. For fits to unfiltered data, a second goodness-of-fit parameter, *F-factor*, was defined as $[\sum k^6(\chi_{exptl} - \chi_{calc})^2/\sum k^6\chi_{exptl}^2]^{1/2}$. In order to account for the effect that additional shells have on improving the fit quality, a third goodness-of-fit metric F' was employed. $F' = F^2/(N_{IDP} - N_{VAR})$, where N_{VAR} is the number of floated variables in the fit and N_{IDP} is the number of independent data points and is defined as $N_{IDP} = 2\Delta k\Delta r/\pi$. In the latter equation, Δk is the k range over which the data is fit, while Δr is the back-transformation range employed in fitting of the Fourier-filtered data. F' is thus of principal utility in fitting of the Fourier-filtered data but can also be employed for unfiltered data by assuming a large value of Δr.

Preedge analysis was performed on data normalized in the *Ifeffit* program *Athena*,[59] and preedge features were fit using the program *Fityk*[60] with Gaussian functions and a pseudo-Voigt baseline function composed of a 50:50 Gaussian/Lorentzian function.

Electron Paramagnetic Resonance (EPR) and Mössbauer Spectroscopies. Mössbauer spectra were recorded with two spectrometers, using Janis Research Super-Varitemp dewars that allowed studies in applied magnetic fields up to 8.0 T in the temperature range from 1.5 to 200 K. Mössbauer spectral simulations were performed using the *WMOSS* software package (WEB Research, Edina, MN). Isomer shifts are quoted relative to iron metal at 298 K. X-band EPR spectra were obtained on a Bruker Elexsys E-500 spectrometer equipped with an Oxford ESR-910 cryostat and an Oxford temperature controller. Data collection was carried out using Xepr (Bruker), and spin quantification was carried out using either Xepr or SpinCount (available courtesy of Professor Michael P. Hendrich of the Department of Chemistry at Carnegie Mellon University).

RESULTS AND DISCUSSION

Structural and Spectroscopic Characterization of $[Fe^{III}_2(\mu\text{-}O)(\mu\text{-}O_2)(BnBQA)_2(NCMe)_2]$ (3). The synthesis and physical properties of the mono- and dinuclear complexes, $[Fe^{II}(BnBQA)(NCMe)_2(OTf)](OTf)$ (**1**) and $[Fe^{II}_2(\mu\text{-}OH)_2(BnBQA)_2(NCMe)_2]^{2+}$ (**2**), have previously been described, along with the initial characterization of the oxygenation product, **3**.[44] Briefly, **2** was shown to exhibit a limited shelf-life and limited solubility in MeCN but was readily generated in situ from the mononuclear complex **1** by treatment with 1 equiv of base/H_2O (relative to **1**). Oxygenation of **2** at −40 °C resulted in the formation of a metastable green intermediate (**3**, $t_{1/2}$ = 6 h at −40 °C), which exhibits three electronic absorption features at 505, 650, and 850 nm ($\varepsilon \sim$ 1250, 1300, and 300 M^{-1} cm^{-1}; Figure 1) that are

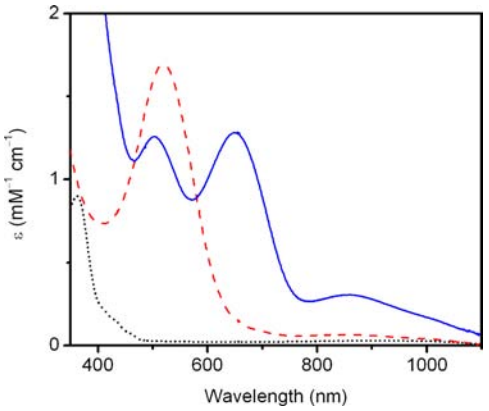

Figure 1. UV–vis absorption spectra of **1** (black dotted line), **2** (red dashed line), and **3** (blue solid line) in MeCN at −40 °C.

characteristic of complexes with $[Fe^{III}_2(\mu\text{-}O)(\mu\text{-}O_2)(L)_2]$ cores.[44] Because a detailed characterization of this complex has not been reported, it is presented here to provide a basis for a comprehensive comparison of its spectral and metrical properties to those of other $[Fe^{III}_2(\mu\text{-}O)(\mu\text{-}O_2)(L)_2]$ complexes and intermediates generated herein.

Additional data have been collected to confirm the identity of **3**, including ESI-MS, Mössbauer, EPR, rRaman, and X-ray absorption spectroscopies. Low-temperature ESI-MS of **3** exhibits a parent $[M^+]$ peak at m/z 1086.8, which can be formulated as $[2Fe^{III} + O^{2-} + O_2^{2-} + 2\ L + OTf^-]^+$ and is consistent with the observed isotope distribution pattern (Figure S1 in the Supporting Information). $^{18}O_2$ labeling of **3** confirms that both O atoms of O_2 are incorporated as shown by the increase in m/z of 4 au. The incorporation of both O atoms of O_2 and the requirement of Fe ions in the molecular formulation suggest that a peroxodiferric complex has been formed; this complex is thus formulated as $[Fe^{III}_2(\mu\text{-}O)(\mu\text{-}O_2)(BnBQA)_2]^{2+}$.

The rRaman spectrum of **3** obtained with λ_{ex} = 647.1 nm exhibits features at 460, 511, 523, 714, and 854 cm^{-1} (Table 2). $^{18}O_2$ labeling of **3** leads to shifts in the 460, 511, and 854 cm^{-1} peaks, whereas $H_2{}^{18}O$ labeling leads to shifts in the 523 and 714 cm^{-1} peaks (Figure 2, top). The shift in the 460 cm^{-1} peak

dx.doi.org/10.1021/ic301642w | Inorg. Chem. 2012, 51, 10417–10426

Table 2. rRaman Features of 3 and 4 and Related Peroxodiferric Complexes[a]

complex	ν(O−O) [Δ^{18}O, $\Delta^{18}O_2$]	ν_{sym}(Fe−O_2−Fe) [Δ^{18}O, $\Delta^{18}O_2$]	ν_{asym}(Fe−O_2−Fe) [Δ^{18}O, $\Delta^{18}O_2$]	ν_{sym}(Fe−O(H)−Fe) [Δ^{18}O, $\Delta^{18}O_2$]	ν_{asym} (Fe−O(H)−Fe) [Δ^{18}O, $\Delta^{18}O_2$]
3	854 [0, −47]	460 [0, −13]	511 [0, −19]	523 [−16, 0]	714 [−42, −]
4	928 [−2, −53]	468 [0, −6]	550 [−4, −17]	424 [−7, −11]	
A	847 [0, −44]	463 [−, −21]	533 [−, −25]	511 [−12, −]	696 [−30, −6]
B	830 [0, −]			537 [−20, −]	
C	847 [−, −33]	465 [−, −19]			695 [−, −2]
C′	908 [−, −47]	460 [−, −13]	548 [−, −18][e]	498 [−, −5]	
D[b]	844 [0, −44]	464 [0, −17]	523 [0, −20]	522 [−13, 0]	708 [−32, −4]
E[c]	853 [0, −45]	463 [0, −15]	529 [0, −26]	510 [−16, 0]	698 [−31, −4]
HPTB-1	900 [−, −50]	471 [−, −16]			
HPTB-2	849 [−, −42]	470 [−, −15]			
HPTB-3	897 [−, −49]	477 [−, −19]			
HPTB-4[d]	845 [−, −49]	464 [−, −21]			
Tp	876 [−, −48]	421 [−, −12]			

[a]See Table 1 for previous definitions and references. [b]**D** = $[Fe^{III}_2(\mu\text{-}O)(\mu\text{-}O_2)(BQPA)_2]^{2+}$ [BQPA = bis(2-quinolylmethyl)-*N*-2-pyridylmethylamine].[49] [c]**E** = $[Fe^{III}_2(\mu\text{-}O)(\mu\text{-}O_2)(6\text{-Me-BQPA})_2]^{2+}$ [6-Me-BQPA = bis(2-quinolylmethyl)(6-methylpyridyl-2-methyl)amine].[49] [d]**HPTB-4** = $[Fe^{III}_2(\mu\text{-}O_2)(N\text{-Et-HPTB})(O_2AsMe_2)(NCMe)]^{2+}$.[50] [e]We reassigned this feature on the basis of its large $\Delta^{18}O_2$ and by comparison with **4**.

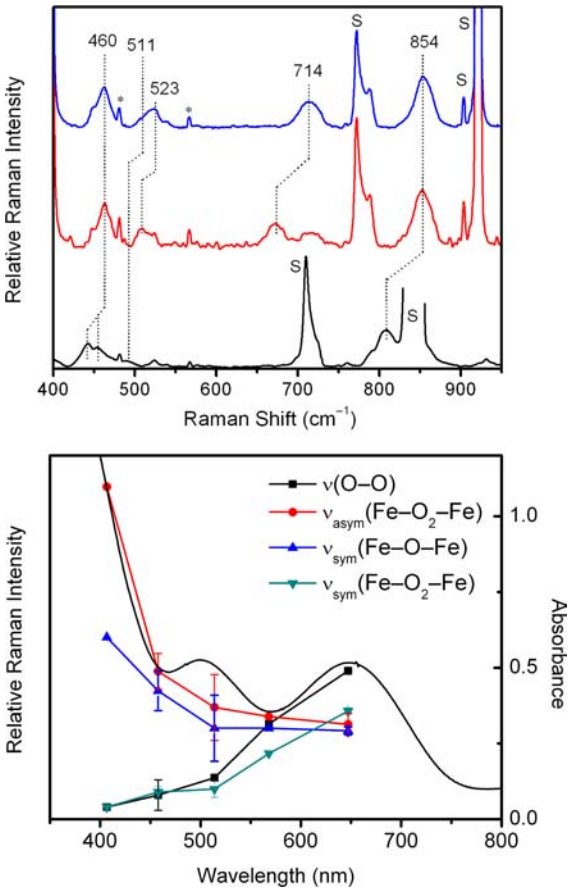

Figure 2. Top: rRaman spectrum of **3** prepared with natural abundance isotopes (top, blue line, MeCN), $H_2{}^{18}O$ (middle, red line, MeCN), and $^{18}O_2$ (bottom, black line, CD_3CN). Spectra were collected at 77 K with λ_{ex} = 647.1 nm, 100 mW, and 6 mM $[Fe]_T$. Solvent peaks are labeled "S", and asterisks denote laser plasma lines. Shifts observed upon ^{18}O labeling can be found in Table 2. Bottom: rRaman excitation profile of **3** showing that the visible absorption features derived from peroxo-to-iron charge-transfer transitions.

upon $^{18}O_2$ labeling leads to the appearance of two peaks at 442 and 453 cm^{-1}, which can be attributed to a Fermi doublet (ν^0 = 447 cm^{-1}). The observed shifts upon ^{18}O labeling are in accordance with those predicted by Hooke's law for a diatomic harmonic oscillator. The peak positions for these resonance-enhanced vibrations are similar to those of previously characterized $[Fe^{III}_2(\mu\text{-}O)(\mu\text{-}O_2)(L)_2]$ complexes[49] and can be assigned to the ν_{sym}(Fe−O_2−Fe), ν_{asym}(Fe−O_2−Fe), ν_{sym}(Fe−O−Fe), ν_{asym}(Fe−O−Fe), and ν(O−O) in order of increasing energy. The excitation profile of **3** (Figure 2, bottom) demonstrates that the O_2^{2-}-related vibrations are associated with the 505 and 650 nm absorption bands and confirms that these features arise from $O_2^{2-} \rightarrow Fe^{III}$ charge-transfer transitions, as previously shown for similar $[Fe^{III}_2(O)(O_2)(L)_2]$ complexes.[49] The contribution of the $O_2^{2-} \rightarrow Fe^{III}$ charge transfer to the UV−vis absorption spectrum of **3** is also evident from the excitation profile because the intensities of ν_{sym}(Fe−O−Fe) and ν_{asym}(Fe−O−Fe) increase with increasing excitation energy. Previously, the energies of ν_{sym}(Fe−O−Fe) and ν_{asym}(Fe−O−Fe) have been shown to correlate with ∠Fe−O−Fe;[61,62] on the basis of this correlation, the ∠Fe−O−Fe angle of **3** can be estimated to be 120°, which is consistent with the Fe···Fe separation determined by EXAFS analysis (vide infra).

Complex **3** is EPR-silent in MeCN at T = 2.5 K, suggesting an antiferromagnetically coupled diiron(III) center (S_T = 0). The spin state and identity of **3** were confirmed by Mössbauer spectroscopy, which showed that oxygenation of **2** results in its near-quantitative conversion (>90%) to **3**. The system can be described by the Hamiltonian (this is the uncoupled representation):

$$\hat{H} = J\hat{S}_1\cdot\hat{S}_2 + \sum_{i=1,2}\{2\beta\hat{S}_i\cdot\hat{B} + A_0\hat{S}_i\cdot\hat{I}_i - g_n\beta_n\hat{B}\cdot\hat{I}_i + H_Q(i)\} \quad (1)$$

where i = 1, 2 sums over the two high-spin Fe^{III} sites ($S_1 = S_2 = {}^5/_2$) and where $H_Q(i)$ describes the quadrupole interaction. Here we neglect the zero-field splittings of the nonheme high-spin ferric sites because these are typically very small (<2 cm^{-1}) for octahedral N/O coordination geometries, as cited in the treatment by Vu et al.[5] The 4.2 K Mössbauer spectrum of **3** consists of one quadrupole doublet in zero field (Figure 3A) with δ = 0.54(1) mm s^{-1} and ΔE_Q = +1.43(2) mm s^{-1}, similar to those previously determined for antiferromagnetically coupled complexes having a $[Fe^{III}_2(\mu\text{-}O)(\mu\text{-}1,2\text{-}O_2)]$ core.[36]

dx.doi.org/10.1021/ic301642w | Inorg. Chem. 2012, 51, 10417−10426

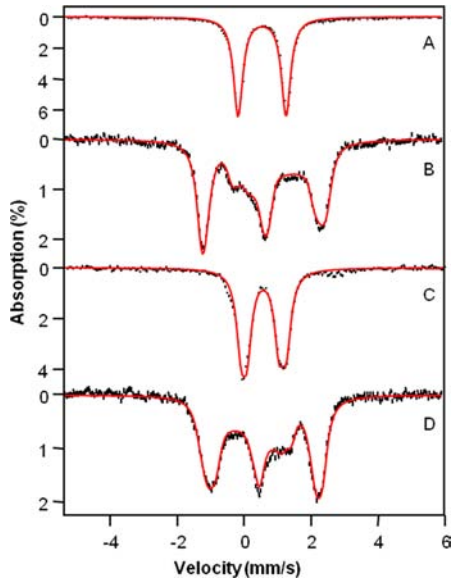

Figure 3. 4.2 K Mössbauer spectra of **3** (A, 0 T; B, 8.0 T) and **4** (C, 0 T; D, 8.0 T) recorded for (parallel) applied magnetic fields. Red lines are simulations based on eq 1, using the parameters listed in Table 1. For the asymmetry parameters, η, of the quadrupole interaction, we obtained $\eta_1 \approx \eta_2 = 0.4 \pm 0.2$ for **3** and $\eta_1 \approx \eta_2 = 0.2 \pm 0.2$ for **4**.

Variable-temperature Mössbauer spectra recorded in applied fields of 8.0 T suggest that $J > 120$ cm^{-1}, indicative of an oxo-bridged diferric complex (160−240 cm^{-1}). (All J values are listed for the $H = JS_1 \cdot S_2$ convention.)[63]

XAS of **3** at the Fe K-edge was carried out to gain insight into the structure of the diiron core because attempts to crystallize **3** were unsuccessful. In the X-ray absorption near-edge region of **3**, the first inflection point of the rising edge was assigned as the edge energy (E_0), which represents the photoionization of a Fe 1s electron to the continuum. For **3**, E_0 was found to be 7124.2 eV, which is 0.6−1.5 eV higher in energy than those reported for related complexes by Fiedler et al.[49] but is typical for high-spin iron(III) centers. There is also a preedge feature that is associated with the dipole-forbidden 1s → 3d transition, which gains significant intensity as the Fe center deviates from centrosymmetry, allowing the Fe 3d and 4p orbitals to mix. For **3**, the preedge feature can be fit with one peak centered at 7114.4 eV with an area = 15.1(6) (Figure S2 in the Supporting Information, top), a value that is smaller than those reported previously for related complexes,[49] suggesting that the Fe centers in this complex are somewhat less distorted from centrosymmetry.

Extended X-ray absorption fine structure (EXAFS) analysis of **3** was carried out to characterize the iron coordination sphere and determine the Fe···Fe distance. Fitting of the EXAFS data reveals scatterers at 1.81, 1.92, 2.21, 3.16, and 2.99 Å (Figure 4 and Table 3), which are consistent with those previously determined for complexes with $[Fe^{III}_2(\mu\text{-O})(\mu\text{-O}_2)]$ cores.[49] These scatterers can be respectively assigned to the oxo bridge, the peroxo bridge, the BnBQA donor atoms, an Fe atom, and second-shell C scatterers from the supporting BnBQA ligand. It should be noted, however, that the difference between the 1.81 and 1.92 Å distances is just under the resolution (0.12 Å for k = 2−15 Å^{-1}) of the EXAFS data. Nevertheless, inclusion of the longer Fe−O distance at 1.92 Å significantly improves the goodness of fit for the data (Table 3; compare Fit 4 vs Fit 5). Thus, this detailed spectroscopic

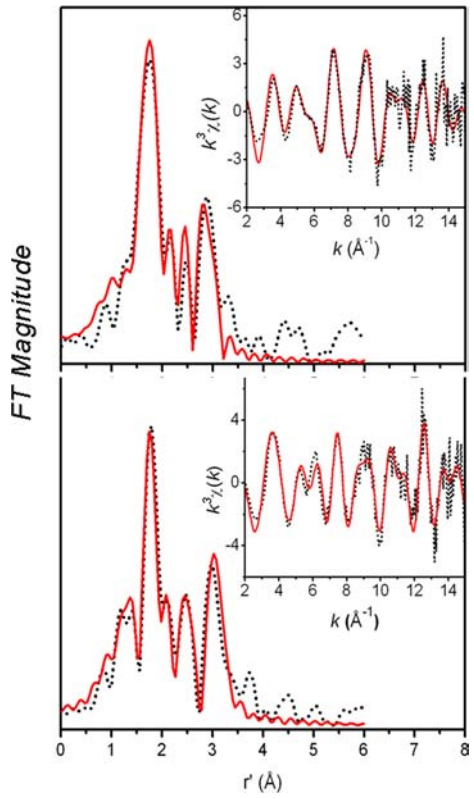

Figure 4. Fourier transform (FT) of the Fe K-edge EXAFS data [$k^3\chi(k)$] and EXAFS spectrum [$k^3\chi(k)$, inset] of **3** (top) and **4** generated with $HClO_4$ (bottom). EXAFS and FT experimental data are shown as dotted black lines and the best fits as solid red lines. The back-transformation range of **3** is ∼0.6−3.95 Å; the FT range is k = 2.0−15 Å^{-1}, while that for **4** is ∼0.6−3.5 Å and the FT range is k = 2−15 Å^{-1}. Fit parameters for **3** (Fit 5) and **4** (Fit 4) are listed in Table 3.

analysis of **3** is consistent with the peroxodiferric designation of Kryatov et al.[44] and insights derived from a recent review of the spectral properties of $[Fe^{III}_2(\mu\text{-O})(\mu\text{-O}_2)(L)_2]$ complexes by Fiedler et al.[49]

Protonation of 3. It has previously been shown that the reaction of $[Fe^{III}_2(\mu\text{-O})(\mu\text{-O}_2)(6\text{-Me}_3\text{-TPA})_2]$ with $HClO_4$ in CH_2Cl_2 yielded a high-valent $[Fe^{III}Fe^{IV}]$ species in 30−35% yield as determined by EPR spectroscopy, with no evidence reported for a protonated derivative prior to formation of the high-valent species.[52,64] In this study, we observe that the reaction of **3** in MeCN at −40 °C with $HClO_4$ results in a UV−vis absorption change from the double-humped feature of **3** to a bathochromically shifted broad absorption centered at 730 nm (ε = 3000 M^{-1} cm^{-1}; Figure 5) associated with this new intermediate, **4**. This intermediate has a half-life of 40 min at −40 °C, and the protonation of **3** can be reversed by neutralization of the added acid with tetramethylimidazole.

EPR and Mössbauer studies of **4** confirm that the diferric core of **3** is retained upon protonation. Complex **4** is EPR-silent at $T \approx 2.5$ K, consistent with retention of an antiferromagnetically coupled diferric core. The Mössbauer spectra exhibit contributions from two quadrupole doublets at low field with δ = 0.57 mm s^{-1} and ΔE_Q = −1.35 mm s^{-1} and δ = 0.56 mm s^{-1} and ΔE_Q = −0.96 mm s^{-1}, respectively (Figure 3C). These doublets account for the formation of **4** in ≈90% yield, along with a minor high-spin ferrous contaminant (5−7%) that can be attributed to **1**. Applied-field Mössbauer spectra of **4** (Figure 3D) confirm the antiferromagnetically coupled nature of the

dx.doi.org/10.1021/ic301642w | Inorg. Chem. 2012, 51, 10417−10426

Table 3. EXAFS Fitting Results for 3 and 4[a]

		Fe−N/O			Fe−O			Fe···Fe			Fe−C			Fe−O					
	fit	N	r (Å)	σ^2	N	r (Å)	σ^2	N	r (Å)	σ^2	N	r (Å)	σ^2	N	r (Å)	σ^2	E_0	F	F'
3	1	6	2.21	7.4													−2.85	660	0.895
	2	4	2.22	4.4	1	1.85	2.7										4.24	310	0.613
	3	4	2.23	4.5	1	1.85	2.8	1	3.19	3.7							5.76	254	0.555
	4	4	2.21	4.2	1	1.84	3	1	3.18	2.7	6	3	6.7				2.2	223	0.522
	5	***4***	***2.21***	***3.8***	***1***	***1.81***	***2.6***	***1***	***3.16***	***2.7***	***4***	***2.99***	***2.5***	***1***	***1.92***	***5.6***	***1.47***	***179***	***0.467***
4	1	6	2.19	11.4													4.39	596	0.830
	2	4	2.18	4.4	1	1.91	2.7										2.01	361	0.646
	3	4	2.17	4.4	1	1.91	2.7	1	3.42	2							0.53	251	0.539
	4	***4***	***2.17***	***3.4***	***2***	***1.91***	***7.7***	***1***	***3.41***	***2.0***	***4***	***2.94***	***3.0***				***-0.73***	***187***	***0.464***
	5	4	2.16	3.4	1	1.95	3.7	1	3.41	2.1	3	2.93	1.5	1	1.87	5	−2.68	165	0.436

[a] k range = 2−15 Å^{-1} for **3** and **4**, resolution = 0.12 Å, and back-transform range ~0.6−3.5 Å for **3** and ~0.6−3.95 Å for **4**. σ^2 = mean-squared deviation in units of 10^{-3} Å^2. Scale factor S_0^2 = 0.9. GOF = goodness of fit calculated as $F = (\sum k^6(\chi_{exp} - \chi_{calc})^2)^{1/2}$. $F' = (\sum k^6(\chi_{exp} - \chi_{calc})^2 / \sum k^6(\chi_{exp})^2)^{1/2}$.

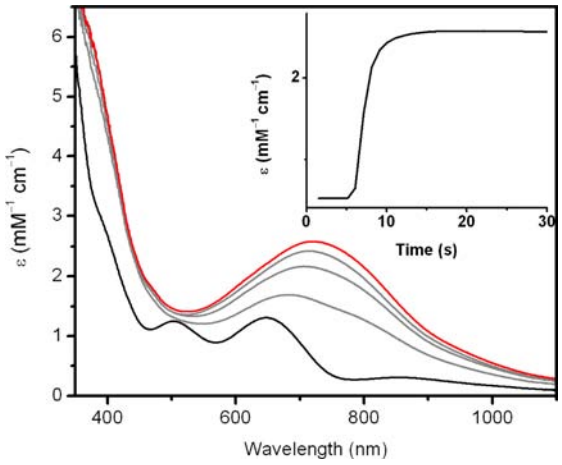

Figure 5. UV−vis absorption changes to **3** (black) upon the addition of 2 equiv of $HClO_4$ (red) in MeCN at −40 °C to form **4**. Intermediate spectra represent data obtained at 6, 7, and 8 s after the addition of acid. Inset: Time course for the increase in the 730 nm absorbance upon the addition of 2 equiv of $HClO_4$.

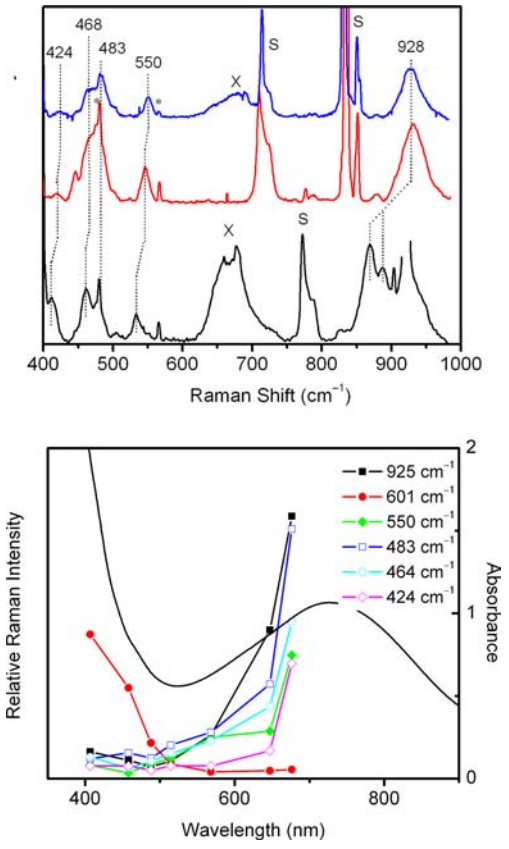

Figure 6. Top: rRaman spectra of **4** generated with 2 equiv of $HClO_4$ and prepared with natural abundance isotopes (top, blue line, CD_3CN), $H_2{}^{18}O$ (middle, red line, MeCN), and $^{18}O_2$ (bottom, black line, MeCN). Spectra were collected at 77 K with λ_{ex} = 647.1 nm, 40 mW, and 6 mM $[Fe]_T$. Solvent peaks are labeled with "S", laser plasma lines are labeled with asterisks, and the "X" denotes notch filter leakage. Bottom: Excitation profile of **4** demonstrating that the 730 nm absorption band is due to an $O_2^{2-} \rightarrow Fe^{III}$ charge-transfer transition.

diferric core, and the exchange coupling between the Fe^{III} centers was determined to be $J = 80 \pm 15$ cm^{-1} from analysis of the temperature dependence of the spectra. The change in J coupling upon conversion of **3** to **4** suggests protonation of the oxo bridge of **3**,[63] which reduces the effectiveness of the oxo bridge as a superexchange pathway between the Fe centers. Furthermore, the observed J value of **4** suggests that the μ-1,2-peroxo bridge remains intact because exchange-coupling values reported for hydroxo-bridged diferric complexes are in the range of $J \sim 14-34$ cm^{-1}.[63] In contrast, $[Fe^{III}{}_2(\mu\text{-}1,2\text{-}O_2)(Tp^{iPr2})_2(\mu\text{-}O_2CC_6H_5)_2]$, which lacks a single-atom bridge, exhibits an antiferromagnetic coupling interaction with J = 66 cm^{-1} that is mediated by the μ-1,2-peroxo bridge.[38]

The rRaman spectrum of **4** with λ_{ex} = 647.1 cm^{-1} exhibits enhanced features at 424, 468, 550, and 928 cm^{-1} in resonance with the 730 nm absorption band of **4** (Figure 6, top). Unlike for **3**, $^{18}O_2$ labeling of **4** led to shifts in all four rRaman features, while $H_2{}^{18}O$ labeling only gave rise to small shifts in the 424, 550, and 928 cm^{-1} peaks (Table 2). The shifts predicted by Hooke's law for a diatomic harmonic oscillator upon ^{18}O labeling show that only the 928 cm^{-1} peak exhibits the expected shift. Thus, the 928 cm^{-1} peak of **4** can be assigned to a "pure" ν(O−O) mode and, to our knowledge, is the highest frequency observed to date for a peroxodiferric complex. The smaller shifts observed for the other features likely arise from significant mechanical coupling between the Fe−OH−Fe and Fe−O_2−Fe modes. In support, the excitation profile of **4** shows that all of these features are resonance-enhanced with the 730 nm absorption band of **4** and leads to the assignment of this absorption feature as an $O_2^{2-} \rightarrow Fe^{III}$ charge-transfer transition.

dx.doi.org/10.1021/ic301642w | Inorg. Chem. 2012, 51, 10417−10426

A fifth feature at 483 cm^{-1} is also in resonance with the 730 nm band but is not ^{18}O-sensitive. The rRaman excitation profile of **4** (Figure 6, bottom) shows a sixth feature at 601 cm^{-1}, which only appears upon near-UV excitation. Because labeling with either $H_2{}^{18}O$ or $^{18}O_2$ does not affect the position of this band, we assume this feature to be a ligand mode.

XAS of **4** shows that it exhibits an edge energy of 7123.3 eV and a preedge feature at 7112.4 eV with an area = 13.8(3) (Figure S2 in the Supporting Information, bottom). This edge energy is consistent with the ferric oxidation state being retained in **4**. Protonation of the oxo bridge of **3** also leads to a decrease in the preedge intensity, indicative of an iron coordination environment less distorted from centrosymmetry.

EXAFS analysis of **4** reveals similar absorber−scatterer distances as determined for **3**, except for the lengthening of the Fe−μ-O and Fe···Fe distances (Figure 4 and Table 3). Elongation of the Fe···Fe distance by ∼0.3 Å compares well with that observed crystallographically for a [$Fe_2(\mu$-OH)(μ-1,2-O_2)] complex.[45] Protonation of the oxo bridge is further confirmed by a comparison of the spectroscopic properties obtained herein with those of previously synthesized μ-oxo/hydroxodiferric pairs, which display hypsochromic shifts in their UV−vis absorption bands, decreases in ΔE_Q and J, and a lengthening of the Fe···Fe distance upon protonation.[45,65−69] Thus, we postulate that protonation of the oxo bridge of **3** results in the formation of **4**.

As demonstrated previously by Fiedler et al.,[49] the structural and spectroscopic properties of the ν(O−O) mode and the Fe···Fe distance of the [$Fe^{III}_2(\mu$-1,2-O_2)] core strongly depend on the identity of the bridging ligand. In Figure 7, we have

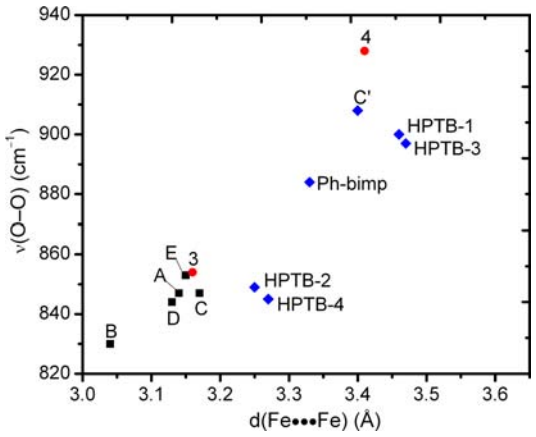

Figure 7. Correlation between the Fe···Fe distance and ν(O−O) for [$Fe^{III}_2(\mu$-1,2-O_2)] complexes with an oxo bridge (black squares) or a hydroxo or alkoxo bridge (blue diamonds). **3** and **4** are represented as red circles. See Tables 1 and 2 for the formulas of the complexes represented by **A**, **B**, **C**, **C′**, **D**, **E**, **Ph-bimp**, **HPTB-1**, **HPTB-2**, **HPTB-3**, and **HPTB-4**.

added data to this correlation plot that have been obtained after 2008, namely, data for **3**, **4**, and the [$Fe^{III}_2(\mu$-1,2-O_2)(N-Et-HPTB)(L1)(L2)] complexes reported by Frisch et al.[50] The value for **3** falls into the tight cluster of points associated with complexes having [$Fe^{III}_2(\mu$-O)(μ-1,2-O_2)] cores (**A**/**A′**−**E**), which have similar ν(O−O) and Fe···Fe values and attest to the rigidity of the [$Fe^{III}_2(\mu$-O)(μ-1,2-O_2)] core. In addition, the inclusion of data for **4** and the HPTB complexes significantly augments the information previously available for complexes with a hydroxo or alkoxo bridge (**C′**, **HPTB-1**, and **Ph-bimp**) and shows that this subset exhibits a much larger range of ν(O−O) and Fe···Fe values, a variability that likely reflects the greater flexibility of the [$Fe^{III}_2(\mu$-OR)(μ-1,2-O_2)] (R = H, alkyl, or aryl) core. Nevertheless, when all of the data are taken together (Figure 7), there remains a general trend where higher ν(O−O) frequencies correspond to longer Fe···Fe distances that should be useful for the estimation of the Fe···Fe distance of a peroxodiferric complex for which its ν(O−O) value has been observed. A significant outlier in this correlation, however, is [$Fe^{III}_2(\mu$-1,2-O_2)(Tp^{iPr2})$_2(\mu$-$O_2CCH_2Ph)_2$] (not plotted in Figure 7), where the peroxodiferric unit is supported only by two μ-1,3-carboxylate bridges. The crystal structure of this complex reveals an Fe···Fe distance of 4.0 Å, but its ν(O−O) value of 876 cm^{-1} falls among values for μ-hydroxo/alkoxo complexes with shorter Fe···Fe distances.[38]

Generation of a High-Valent Species (5). Complex **4** generated from the addition of $HClO_4$ to **3** decomposes over the course of a few hours at −40 °C ($t_{1/2}$ = 40 min). However, this decay process appears complicated and does not proceed along a single-exponential pathway. Furthermore, there is only a small amount (<3% yield on a diiron basis) of an isotropic $S = {}^1/_2$ EPR signal at g = 2 that is observed to form and may be associated with an Fe^{III}−O−Fe^{IV} species (**5**), as reported previously upon the treatment of [$Fe^{III}_2(\mu$-O)(μ-1,2-O_2)(6-Me_3TPA)$_2$]$^{2+}$ with $HClO_4$.[52]

The story is quite different when HNO_3 is used in place of $HClO_4$ to generate **4** from **3**. Although the addition of 1 equiv of HNO_3 to a solution of **3** elicits the same UV−vis and rRaman features associated with the formation of **4** (Figures S3 and S4 in the Supporting Information), the lifetime of **4** under these conditions is much shorter ($t_{1/2}$ = 140 s vs 40 min at −40 °C). As shown in Figure 8, its decay proceeds through an

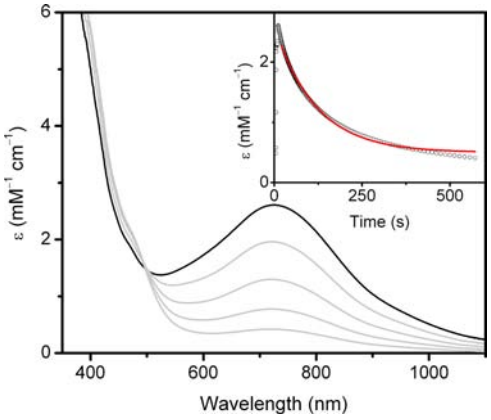

Figure 8. Generation of **4** in CH_3CN with 1 equiv of HNO_3 at −40 °C and its subsequent decay. Inset: Decrease in the 730 nm absorption band as a function of time, along with the best-fit line (red).

isosbestic point at 500 nm, leading to the formation of a pale-yellow solution, and can be fit with a first-order exponential function for a large fraction of the process. Under these conditions, the decay of **4** elicits a substantially more intense isotropic EPR signal at $g \sim 2$, which exhibits considerable line broadening with the introduction of ^{57}Fe (Figure 9). This observation is similar to that reported by Xue et al.[70] for a mixed-valent [Fe^{III}−O−Fe^{IV}] complex, consistent with the $S_T = {}^1/_2$ signal arising from an antiferromagnetically coupled $Fe^{III}Fe^{IV}$ center. Warming the EPR sample to room temperature and subsequent refreezing resulted in the disappearance

dx.doi.org/10.1021/ic301642w | Inorg. Chem. 2012, 51, 10417−10426

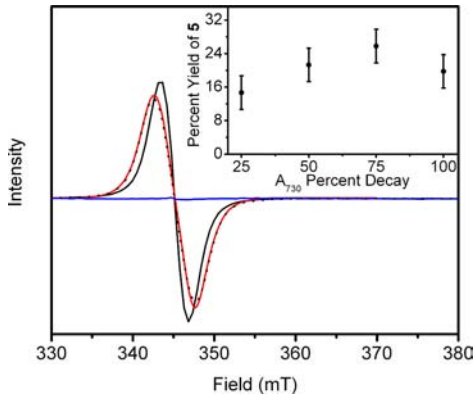

Figure 9. X-band EPR spectra of 0.5 mM **5** in MeCN at $T \approx 2.5$ K using ^{56}Fe (black) and ^{57}Fe (red); the blue trace was obtained for the ^{57}Fe sample after warming to room temperature. The black dotted line is a simulation of the ^{57}Fe sample of **5** using the spectral parameters reported in ref 71 (Figure S5 in the Supporting Information). Inset: Percentage of diiron clusters observed in the $S_T = {}^1/_2$ EPR state of **5** versus the percent decay of the 730 nm chromophore associated with **4**. Conditions: 9.645 GHz; microwave power, 0.02 mW; modulation, 1 mT.

of the $g \sim 2$ signal accompanied by a small increase in the $g = 4.3$ feature due to high-spin Fe^{III}. The intensity of the isotropic $g = 2$ signal of **5** at various time points during the decay of **4** did not change dramatically, ranging from 16 to 24% of the total diiron content of the sample (Figure 9, inset). Increasing the amount of acid added results in a drastic decrease in the amount of **5** observed by EPR (<5%), showing that **5** is acid-sensitive as well. These observations suggest that the formation and decay rates of **5** are comparable under these conditions so that what we observe by EPR is a steady-state concentration of **5** of about 20% of the total diiron content of the sample.

The Mössbauer spectrum of a sample frozen after 90% of **4** had decayed exhibits for $B = 50$ mT a quadrupole doublet with parameters indicative of a diferric complex. This doublet representing ca. 80% of Fe is comprised of two (slightly) inequivalent sites with $\delta = 0.48$ mm s^{-1}, $\Delta E_Q = -1.24$ mm s^{-1} and $\delta = 0.52$ mm s^{-1}, $\Delta E_Q = -1.34$ mm s^{-1}, respectively. The 8.0 T spectrum of the sample, shown in Figure 10, shows that the 80% component has $S = 0$, indicating an antiferromagnetically coupled diiron(III) species. Partly masked by this species is the spectrum (ca. 20% of Fe) of **5**, which corresponds to the

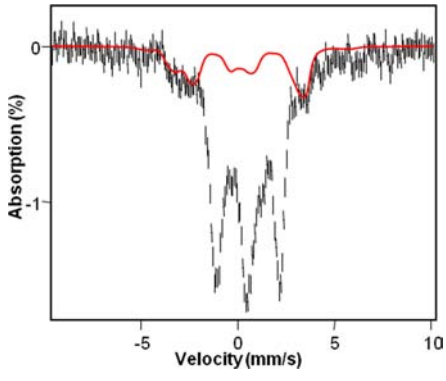

Figure 10. 8.0 T Mössbauer spectrum observed at 4.2 K of a sample frozen after **4** was 90% decayed. The red line is a simulation for an antiferromagnetically coupled Fe^{III}Fe^{IV} complex with $S_T = {}^1/_2$, using parameters of the Fe^{III}Fe^{IV} complex described by De Hont et al.[71]

mixed-valent [Fe^{III}–O–Fe^{IV}] complex. We have simulated this species (red line in Figure 10) using the parameters of the $S_T = {}^1/_2$ [Fe^{III}–O–Fe^{IV}] complex studied by De Hont et al.[71] (Note: The observation of an isotropic $S = {}^1/_2$ EPR signal representing about 20% of the Fe$_2$ centers and exhibiting ^{57}Fe broadening must be associated with a Mössbauer spectrum exhibiting a paramagnetic hyperfine structure. The feature outlined by the red line is the only viable candidate fulfilling this requirement.) Overall, the EPR and Mossbauer data support the formation of an antiferromagnetically coupled [Fe^{IV}–O–Fe^{III}] from **4**, demonstrating that the protonation of **3** results in O–O bond cleavage. The fraction of diiron clusters observed in the $S_T = {}^1/_2$ Fe^{III}Fe^{IV} state is in good agreement with the EPR results of Figure 9, which show that roughly 20% of the clusters are in this state as we follow the decay of **4**.

Thus, there are three important issues that remain unresolved in this study. First, we do not know why $HClO_4$ and HNO_3 have such different effects on the decay rate of **4**, despite their similarity in acid strength. Second, we have not yet identified the source of the electron needed to convert the Fe^{III}–O–O–Fe^{III} complex **4** to the Fe^{III}–O–Fe^{IV} complex **5**. Lastly, we have not been able to shed light on the detailed pathway for O–O bond cleavage. Clearly, more work is required to solve these puzzles.

Implications for O_2-Activating Nonheme Diiron Enzymes. In this study, we have demonstrated an example of how a (μ-oxo)(μ-1,2-peroxo)diiron(III) complex can be protonated so as to undergo O–O bond cleavage (Scheme 1).

Scheme 1. Conversion of the Diiron(II) Precursor 2 to the Fe^{III}–O–Fe^{IV} Complex 5 via Peroxodiferric Intermediates 3 and 4

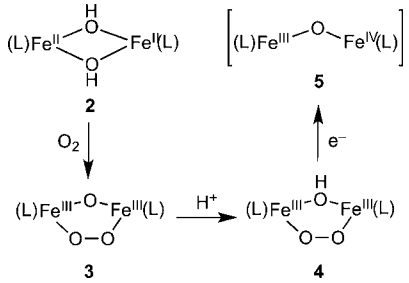

Oxygenation of the bis(μ-hydroxo)diiron(II) complex of the tridentate BnBQA ligand (**2**) results in the formation of a relatively stable O_2 adduct **3** that has been characterized to have an [Fe$^{III}_2$(μ-O)(μ-1,2-O$_2$)] core.[44] The addition of strong acid affords **4** with an [Fe$^{III}_2$(μ-OH)(μ-1,2-O$_2$)] core, which, in turn, decays to give rise to a species (**5**) with a $S_T = {}^1/_2$ signal attributable to an [Fe^{III}–O–Fe^{IV}] species. This model system can provide useful insight into how corresponding O–O bond cleavage steps may occur in nonheme diiron enzymes.

To date, peroxodiferric intermediates have been trapped for several nonheme diiron enzymes, including sMMO,[20−22] W48F/D84E RNR R2,[23−26] Δ^9D,[30,31] frog M ferritin,[28,56] and hDOHH.[5] These intermediates have been identified by visible absorption and Mössbauer spectroscopy and, in some cases, further characterized by rRaman spectroscopy and EXAFS analysis. Interestingly, these intermediates exhibit lifetimes that range from days to less than a second. For example, the hDOHH peroxo intermediate (hDOHH$_{peroxo}$) has the longest lifetime observed thus far, with a $t_{1/2}$ of days at 25

dx.doi.org/10.1021/ic301642w | Inorg. Chem. 2012, 51, 10417−10426

°C in the absence of a substrate.[5] The addition of its protein substrate effects a dramatic decrease in its lifetime to hours, resulting in hydroxylation of the deoxyhypusine amino acid residue on the substrate. This result suggests that $hDOHH_{peroxo}$ is not a dead-end species but one involved in the hDOHH catalytic cycle; however, additional factors not yet identified are likely to be required to achieve maximum catalytic efficiency. The spectroscopic data for $hDOHH_{peroxo}$ compare well with those of the synthetic complexes in Table 1 with hydroxo or alkoxo bridges and support the presence of a hydroxo bridge for $hDOHH_{peroxo}$, which we suggest is a significant factor in stabilizing this peroxodiferric intermediate.

In contrast, the lifetimes of the other peroxodiferric intermediates are significantly shorter: Δ^9D_{peroxo} (30 min),[30] W48F/D84E RNR $R2_{peroxo}$ (2.7 min),[24] sMMO H_{peroxo} (~1 s),[9,20−22,72] and $ferritin_{peroxo}$ (0.17 s).[56] The latter intermediates differ from $hDOHH_{peroxo}$ in having Mössbauer isomer shifts larger than 0.6 mm s^{-1} (Table 1), values that are less typical of high-spin iron(III) centers and suggest the introduction of some ferrous−superoxo character into the electronic description of the peroxodiferric unit. These isomer shifts approach or match that for $[Fe^{III}_2(\mu\text{-}O_2)(Tp^{iPr2})_2(\mu\text{-}O_2CCH_2Ph)_2]$,[41] which is the only synthetic peroxo diferric complex listed in Table 1 that is bridged only by carboxylates. Indeed, density functional theory (DFT) and/or quantum mechanic/molecular mechanic (QM/MM) calculations on Δ^9D_{peroxo},[35] W48F/D84E RNR $R2_{peroxo}$,[26] and sMMO H_{peroxo}[16,17,72−74] calibrated by available spectroscopic data favor a $[Fe^{III}_2(cis\text{-}\mu\text{-}1,2\text{-}O_2)]$ core supported by two carboxylate bridges. It would thus appear that the presence of a hydroxo bridge in $hDOHH_{peroxo}$ leads to a much more stable peroxo intermediate. We speculate that the hydroxo bridge may constrain the peroxodiferric unit from readily undergoing the structural rearrangement required for O−O bond cleavage, thus leading to more stable intermediates. In support, we point out that, among synthetic peroxodiferric complexes, the presence of an additional oxo bridge affords an even more stable species than the presence of an additional hydroxo bridge.

Whatever the core structure for the trapped peroxo intermediates of nonheme diiron enzymes, it appears that protonation can play a significant role in facilitating cleavage of the O−O bond, parallel to the effect of protonation on the lifetimes of **3** and **4**. In the cases of the two sMMOs for which detailed kinetic studies are available,[8,9] the conversion of the peroxo precursor to **Q** was found to be accelerated by lowering the pH of the buffer solution and kinetic solvent (D_2O/H_2O) isotope effects of 1.4−1.8 were observed. Similarly, lowering the pH increased the rate of substrate oxidation by $hDOHH_{peroxo}$.[5] Different modes of action can be postulated depending on the site of the initial protonation. For cytochrome P450, proton delivery is typically carried out by second-sphere distal residues, leading to a Fe^{III}-η^1-OOH intermediate.[75] In nonheme diiron enzymes, protonation may occur directly on the bridging peroxo ligand, leading to its isomerization to a related hydroperoxo intermediate;[17,26,76] however, our studies of synthetic peroxodiferric complexes suggest that the peroxo bridge is the least Lewis basic site. Alternatively, protonation of one of the other ligands on the diiron center, such as a carboxylate or a possible single-atom bridge, may lead to a significant geometrical rearrangement that induces O−O bond cleavage (e.g., loss of a bridging ligand).

A particularly attractive mode of proton delivery in an enzyme active site is via a bridging carboxylate ligand, which was recently suggested by Do et al. on the basis of model studies.[77] They demonstrated reversible protonation of a carboxylate ligand in a synthetic peroxodiferric complex containing both an alkoxo and carboxylato bridge, which resulted in a *small* bathochromic shift (10 nm) of the $O_2^{2-} \rightarrow Fe^{III}$ charge-transfer band. Changes in the ν(COO) value of the carboxylato ligand were also observed, consistent with its protonation, but the ν(Fe−O) and ν(O−O) values associated with the peroxodiferric core were not significantly perturbed. However, it was not reported whether this protonation step affected the stability of the peroxodiferric species. On the other hand, in this study we have demonstrated that protonation of **3** occurs at the oxo bridge to afford **4**, which allows the latter to undergo O−O bond cleavage to generate high-valent **5**. This work may help to explain how the presence of a single-atom bridge increases the stability of $hDOHH_{peroxo}$ compared to other peroxodiferric enzyme intermediates and how protonation can trigger O−O bond cleavage in peroxodiferric intermediates.

■ ASSOCIATED CONTENT

Ⓢ Supporting Information

ESI-MS data of **3**, X-ray absorption preedge spectra of **3** and **4**, UV−vis and rRaman spectra of **4** generated by the addition of 1 equiv of HO_3, and EPR spectra of **5**. This material is available free of charge via the Internet at http://pubs.acs.org.

■ AUTHOR INFORMATION

Corresponding Author

*E-mail: larryque@umn.edu (L.Q.), emunck@cmu.edu (E.M.).

Notes

The authors declare no competing financial interest.

■ ACKNOWLEDGMENTS

We are grateful for the support provided by NIH Grants GM38767 (to L.Q.) and EB001475 (to E.M.), NSF Grant CHE-1012485 (to E.M.), and NIH Postdoctoral Fellowship ES017390 (to M.A.C.). M.A.C. also acknowledges Drs. Erik R. Farquhar and Van V. Vu for helpful discussions. XAS was carried out at the SSRL, a Directorate of SLAC National Accelerator Laboratory and an Office of Science User Facility operated for the U.S. Department of Energy Office of Science by Stanford University. The SSRL Structural Molecular Biology Program is supported by the DOE Office of Biological and Environmental Research and by the National Institutes of Health, National Center for Research Resources, Biomedical Technology Program (P41RR001209).

■ REFERENCES

(1) Colby, J.; Stirling, D. I.; Dalton, H. *Biochem. J.* **1977**, *165*, 395.
(2) Patel, R. N.; Hou, C. T.; Laskin, A. I.; Felix, A. *Appl. Environ. Microbiol.* **1982**, *44*, 1130.
(3) Lipscomb, J. D. *Annu. Rev. Microbiol.* **1994**, *48*, 371.
(4) Wallar, B. J.; Lipscomb, J. D. *Chem. Rev.* **1996**, *96*, 2625.
(5) Vu, V. V.; Emerson, J. P.; Martinho, M.; Kim, Y. S.; Münck, E.; Park, M. H.; Que, L., Jr. *Proc. Natl. Acad. Sci. U.S.A.* **2009**, *106*, 14814.
(6) Makris, T. M.; Chakrabarti, M.; Münck, E.; Lipscomb, J. D. *Proc. Natl. Acad. Sci. U.S.A.* **2010**, *107*, 15391.
(7) Stubbe, J. *Curr. Opin. Chem. Biol.* **2003**, *7*, 183.
(8) Lee, S. Y.; Lipscomb, J. D. *Biochemistry* **1999**, *38*, 4423.
(9) Tinberg, C. E.; Lippard, S. J. *Biochemistry* **2009**, *48*, 12145.
(10) Rova, U.; Adrait, A.; Pötsch, S.; Gräslund, A.; Thelander, L. *J. Biol. Chem.* **1999**, *274*, 23746.

(11) Stubbe, J.; Nocera, D. G.; Yee, C. S.; Chang, M. C. Y. *Chem. Rev.* **2003**, *103*, 2167.
(12) Shu, L.; Nesheim, J. C.; Kauffmann, K.; Münck, E.; Lipscomb, J. D.; Que, L., Jr. *Science* **1997**, *275*, 515−518.
(13) Gherman, B. F.; Baik, M. H.; Lippard, S. J.; Friesner, R. A. *J. Am. Chem. Soc.* **2004**, *126*, 2978.
(14) Rinaldo, D.; Philipp, D. M.; Lippard, S. J.; Friesner, R. A. *J. Am. Chem. Soc.* **2007**, *129*, 3135.
(15) Han, W. G.; Noodleman, L. *Inorg. Chim. Acta* **2008**, *361*, 973.
(16) Han, W.-G.; Noodleman, L. *Inorg. Chem.* **2008**, *47*, 2975.
(17) Bochevarov, A. D.; Friesner, R. A.; Lippard, S. J. *J. Chem. Theory Comput.* **2010**, *6*, 3735.
(18) Bollinger, J. M.; Stubbe, J.; Huynh, B. H.; Edmondson, D. E. *J. Am. Chem. Soc.* **1991**, *113*, 6289.
(19) Sturgeon, B. E.; Burdi, D.; Chen, S. X.; Huynh, B. H.; Edmondson, D. E.; Stubbe, J.; Hoffman, B. M. *J. Am. Chem. Soc.* **1996**, *118*, 7551.
(20) Lee, S.-K.; Nesheim, J. C.; Lipscomb, J. D. *J. Biol. Chem.* **1993**, *268*, 21569.
(21) Liu, K. E.; Valentine, A. M.; Wang, D.; Huynh, B. H.; Edmondson, D. E.; Salifoglou, A.; Lippard, S. J. *J. Am. Chem. Soc.* **1995**, *117*, 10174.
(22) Valentine, A. M.; Stahl, S. S.; Lippard, S. J. *J. Am. Chem. Soc.* **1999**, *121*, 3876.
(23) Bollinger, J. M.; Krebs, C.; Vicol, A.; Chen, S.; Ley, B. A.; Edmondson, D. E.; Huynh, B. H. *J. Am. Chem. Soc.* **1998**, *120*, 1094.
(24) Moënne-Loccoz, P.; Baldwin, J.; Ley, B. A.; Loehr, T. M.; Bollinger, J. M. *Biochemistry* **1998**, *37*, 14659.
(25) Baldwin, J.; Krebs, C.; Saleh, L.; Stelling, M.; Huynh, B. H.; Bollinger, J. M.; Riggs-Gelasco, P. *Biochemistry* **2003**, *42*, 13269.
(26) Skulan, A. J.; Brunold, T. C.; Baldwin, J.; Saleh, L.; Bollinger, J. M.; Solomon, E. I. *J. Am. Chem. Soc.* **2004**, *126*, 8842.
(27) Yun, D.; Garcia-Serres, R.; Chicalese, B. M.; An, Y. H.; Huynh, B. H.; Bollinger, J. M. *Biochemistry* **2007**, *46*, 1925.
(28) Hwang, J.; Krebs, C.; Huynh, B. H.; Edmondson, D. E.; Theil, E. C.; Penner-Hahn, J. E. *Science* **2000**, *287*, 122.
(29) Krebs, C.; Bollinger, J. M., Jr.; Theil, E. C.; Huynh, B. H. *J. Biol. Inorg. Chem.* **2002**, *7*, 863.
(30) Broadwater, J. A.; Ai, J.; Loehr, T. M.; Sanders, L.; Fox, B. G. *Biochemistry* **1998**, *37*, 14664.
(31) Broadwater, J. A.; Achim, C.; Münck, E.; Fox, B. G. *Biochemistry* **1999**, *38*, 12197.
(32) Murray, L. J.; Garcia-Serres, R.; Naik, S.; Huynh, B. H.; Lippard, S. J. *J. Am. Chem. Soc.* **2006**, *128*, 7458.
(33) Song, W. J.; Behan, R. K.; Naik, S. G.; Huynh, B. H.; Lippard, S. J. *J. Am. Chem. Soc.* **2009**, *131*, 6074.
(34) Brunold, T. C.; Tamura, N.; Kitajima, N.; Moro-oka, Y.; Solomon, E. I. *J. Am. Chem. Soc.* **1998**, *120*, 5674.
(35) Srnec, M.; Rokob, T. A.; Schwartz, J. K.; Kwak, Y.; Rulisek, L.; Solomon, E. I. *Inorg. Chem.* **2012**, *51*, 2806.
(36) Tshuva, E. Y.; Lippard, S. J. *Chem. Rev.* **2004**, *104*, 987.
(37) Dong, Y.; Menage, S.; Brennan, B. A.; Elgren, T. E.; Jang, H. G.; Pearce, L. L.; Que, L., Jr. *J. Am. Chem. Soc.* **1993**, *115*, 1851.
(38) Kitajima, N.; Tamura, N.; Amagai, H.; Fukui, H.; Moro-oka, Y.; Mizutani, Y.; Kitagawa, T.; Mathur, R.; Heerwegh, K. *J. Am. Chem. Soc.* **1994**, *116*, 9071.
(39) Dong, Y. H.; Yan, S. P.; Young, V. G.; Que, L., Jr. *Angew. Chem., Int. Ed.* **1996**, *35*, 618.
(40) Ookubo, T.; Sugimoto, H.; Nagayama, T.; Masuda, H.; Sato, T.; Tanaka, K.; Maeda, Y.; Okawa, H.; Hayashi, Y.; Uehara, A.; Suzuki, M. *J. Am. Chem. Soc.* **1996**, *118*, 701.
(41) Kim, K.; Lippard, S. J. *J. Am. Chem. Soc.* **1996**, *118*, 4914.
(42) Costas, M.; Cady, C. W.; Kryatov, S. V.; Ray, M.; Ryan, M. J.; Rybak-Akimova, E. V.; Que, L., Jr. *Inorg. Chem.* **2003**, *42*, 7519.
(43) Kodera, M.; Itoh, M.; Kano, K.; Funabiki, T.; Reglier, M. *Angew. Chem., Int. Ed.* **2005**, *44*, 7104.
(44) Kryatov, S. V.; Taktak, S.; Korendovych, I. V.; Rybak-Akimova, E. V.; Kaizer, J.; Torelli, S.; Shan, X. P.; Mandal, S.; MacMurdo, V. L.; Mairata i Payeras, A.; Que, L., Jr. *Inorg. Chem.* **2005**, *44*, 85.
(45) Zhang, X.; Furutachi, H.; Fujinami, S.; Nagatomo, S.; Maeda, Y.; Watanabe, Y.; Kitagawa, T.; Suzuki, M. *J. Am. Chem. Soc.* **2005**, *127*, 826.
(46) Arii, H.; Funahashi, Y.; Ozawa, T.; Jitsukawa, K.; Masuda, H. *J. Organomet. Chem.* **2007**, *692*, 343.
(47) Kodera, M.; Kano, K. *Bull. Chem. Soc. Jpn.* **2007**, *80*, 662.
(48) Yamashita, M.; Furutachi, H.; Tosha, T.; Fujinami, S.; Saito, W.; Maeda, Y.; Takahashi, K.; Tanaka, K.; Kitagawa, T.; Suzuki, M. *J. Am. Chem. Soc.* **2007**, *129*, 2.
(49) Fiedler, A. T.; Shan, X.; Mehn, M. P.; Kaizer, J.; Torelli, S.; Frisch, J. R.; Kodera, M.; Que, L., Jr. *J. Phys. Chem. A* **2008**, *112*, 13037.
(50) Frisch, J. R.; Vu, V. V.; Martinho, M.; Münck, E.; Que, L., Jr. *Inorg. Chem.* **2009**, *48*, 8325.
(51) Friedle, S.; Kodanko, J. J.; Morys, A. J.; Hayashi, T.; Moenne-Loccoz, P.; Lippard, S. J. *J. Am. Chem. Soc.* **2009**, *131*, 14508.
(52) MacMurdo, V. L.; Zheng, H.; Que, L., Jr. *Inorg. Chem.* **2000**, *39*, 2254.
(53) Kodera, M.; Taniike, Y.; Itoh, M.; Tanahashi, Y.; Shimakoshi, H.; Kano, K.; Hirota, S.; Lijima, S.; Ohba, M.; Okawa, H. *Inorg. Chem.* **2001**, *40*, 4821.
(54) Dong, Y. H.; Zang, Y.; Shu, L. J.; Wilkinson, E. C.; Que, L., Jr.; Kauffmann, K.; Münck, E. *J. Am. Chem. Soc.* **1997**, *119*, 12683.
(55) Murch, B. P.; Bradley, F. C.; Que, L., Jr. *J. Am. Chem. Soc.* **1986**, *108*, 5027.
(56) Moënne-Loccoz, P.; Krebs, C.; Herlihy, K.; Edmondson, D. E.; Theil, E. C.; Huynh, B. H.; Loehr, T. M. *Biochemistry* **1999**, *38*, 5290.
(57) Hagen, K. S. *Inorg. Chem.* **2000**, *39*, 5867.
(58) George, G. N., Stanford Synchrotron Radiation Laboratory, Stanford Linear Accelerator, Stanford, CA, 2000.
(59) Ravel, B. N. M. *J. Synchotron Radiat.* **2005**, *12*, 537.
(60) Wojdyr, M. *J. Appl. Crystallogr.* **2010**, *43*, 1126.
(61) Backes, G.; Sahlin, M.; Sjoberg, B. M.; Loehr, T. M.; Sanders-Loehr, J. *Biochemistry* **1989**, *28*, 1923.
(62) Zheng, H.; Zang, Y.; Dong, Y. H.; Young, V. G.; Que, L., Jr. *J. Am. Chem. Soc.* **1999**, *121*, 2226.
(63) Kurtz, D. M., Jr. *Chem. Rev.* **1990**, *90*, 585.
(64) Dong, Y.; Zang, Y.; Shu, L.; Wilkinson, E. C.; Que, L., Jr.; Kauffmann, K.; Münck, E. *J. Am. Chem. Soc.* **1997**, *119*, 12683.
(65) Armstrong, W. H.; Lippard, S. J. *J. Am. Chem. Soc.* **1984**, *106*, 4632.
(66) Turowski, P. N.; Armstrong, W. H.; Liu, S.; Brown, S. N.; Lippard, S. J. *Inorg. Chem.* **1994**, *33*, 636.
(67) Mizoguchi, T. J.; Davydov, R. M.; Lippard, S. J. *Inorg. Chem.* **1999**, *38*, 4098.
(68) Armentano, D.; De Munno, G.; Mastropietro, T. F.; Julve, M.; Lloret, F. *J. Am. Chem. Soc.* **2005**, *127*, 10778.
(69) Evans, D. R.; Mathur, R. S.; Heerwegh, K.; Reed, C. A.; Xie, Z. *Angew. Chem., Int. Ed.* **1997**, *36*, 1335.
(70) Xue, G.; De Hont, R.; Münck, E.; Que, L., Jr. *Nat. Chem.* **2010**, *2*, 400.
(71) De Hont, R. F.; Xue, G.; Hendrich, M. P.; Que, L., Jr.; Bominaar, E. L.; Münck, E. *Inorg. Chem.* **2010**, *49*, 8310.
(72) Tinberg, C. E.; Lippard, S. J. *Acc. Chem. Res.* **2011**, *44*, 280.
(73) Yumura, T.; Yoshizawa, K. *Bull. Chem. Soc. Jpn.* **2004**, *77*, 1305.
(74) Chachiyo, T.; Rodriguez, J. H. *Dalton Trans.* **2012**, *41*, 995.
(75) Denisov, I. G.; Makris, T. M.; Sligar, S. G.; Schlichting, I. *Chem. Rev.* **2005**, *105*, 2253.
(76) Korboukh, V. K.; Li, N.; Barr, E. W.; Bollinger, J. M., Jr.; Krebs, C. *J. Am. Chem. Soc.* **2009**, *131*, 13608.
(77) Do, L. H.; Hayashi, T.; Moenne-Loccoz, P.; Lippard, S. J. *J. Am. Chem. Soc.* **2010**, *132*, 1273.